Available online at www.sciencedirect.com
ScienceDirect
Journal of Structural Biology 157 (2007) 156–167
Journal of Structural Biology
www.elsevier.com/locate/yjsbi

A novel method for improvement of visualization of power spectra for sorting cryo-electron micrographs and their local areas

S. Jonić [a,*], C.O.S. Sorzano [b], M. Cottevieille [a], E. Larquet [a], N. Boisset [a]

[a] *Institut de Minéralogie et de Physique des Milieux Condensés (IMPMC), Université Pierre et Marie Curie, UMR 7590, CNRS, P7, IPG, 140 rue de Lourmel, 75015 Paris, France*

[b] *Escuela Politécnica Superior, Univ. San Pablo—CEU, Campus Urb. Montepríncipe s/n, 28668 Boadilla del Monte, Madrid, Spain*

Received 31 March 2006; received in revised form 23 June 2006; accepted 28 June 2006
Available online 11 August 2006

Abstract

In a context of automation of cryo-electron microscopy, we developed a novel method for improving visibility of diffraction rings in the power spectra of cryo-electron micrographs of vitreous ice (without carbon film or high concentration of diffracting material). We used these enhanced spectra to semi-automatically detect and remove micrographs and/or local areas introducing errors in the global 3D map (drifted and charged areas) or those unable to increase global signal-to-noise ratio (non-diffracting areas). Our strategy also allows a detection of micrographs/areas with a strong astigmatism. These images should be removed when using algorithms that do not correct astigmatism. Our sorting method is simple and fast since it uses the normalized cross-correlation between enhanced spectra and their copies rotated by 90°. It owes its success mainly to the novel pre-processing of power spectra. The improved visibility also allows an easier visual check of accuracy of sorting. We show that our algorithm can even improve the visibility of diffraction rings of cryo-electron micrographs of pure water. Moreover, we show that this visibility depends strongly on ice thickness. This algorithm is implemented in the Xmipp (open-source image processing package) and is freely available for implementation in any other software package.

Keywords: Sorting; Diffraction rings; Visualization; Power spectrum; Periodogram; Contrast transfer function (CTF); Automation; High resolution; Single-particle reconstruction; Cryo-electron microscopy (cryo-EM)

1. Introduction

Cryo-electron microscopy (cryo-EM) of randomly oriented single particles, when combined with three-dimensional (3D) reconstruction techniques is an efficient method to study the architecture of macromolecular assemblies in their native states (Dubochet et al., 1982; Lepault et al., 1983; Frank, 1996). Automated methods for data collection increase the data quantity that can be collected during a single cryo-EM session (Potter et al., 1999; Carragher et al., 2000; Zhang et al., 2001). These methods combined with techniques for automated particle picking (for review and comparative study, see, Nicholson and Glaeser, 2001; Zhu et al., 2004, respectively) can generate a 3D map at sub-nanometer resolution within 24 h after inserting the specimen grid into the microscope (Zhu et al., 2001).

However, for a high-resolution reconstruction, data quality is as much important as data quantity. Beside sample heterogeneity that can be explored by 3D variance estimation (Grob et al., 2006; Penczek et al., 2006a,b), contrast transfer function (CTF) of electron microscopes is another element that affects attainable resolution of 3D reconstructions (Hanszen, 1971; Lenz, 1971; Spence, 1988; Hawkes, 1992; Wade, 1992; Frank, 1996). Many algorithms have been developed to determine parameters of the CTF for its subsequent correction (Tani et al., 1996; Zhu et al., 1997; Conway and Steven, 1999; Ludtke et al., 1999; Radermacher et al., 2001; Huang et al., 2003; Mindell and Grigorieff, 2003; Sander et al., 2003; Velázquez-Muriel et al., 2003; Mallick et al., 2005). However, since they are based

* Corresponding author. Fax: +33 1 44 27 37 85.
E-mail address: Slavica.Jonic@impmc.jussieu.fr (S. Jonić).

1047-8477/$ - see front matter © 2006 Elsevier Inc. All rights reserved.
doi:10.1016/j.jsb.2006.06.014

on fitting of a CTF model to the power spectrum, they may fail on micrographs with very poorly visible diffraction or Thon rings. This usually happens when recording large vitreous ice areas with no supporting carbon film underneath, or with only a few single particles per cryo-EM image field. Hence, CTF parameter determination is commonly done using the average of the power spectra computed from local areas of a micrograph, under the assumption that local power spectra can be described with the same parameters everywhere in the micrograph, which is often not true (Gao et al., 2002).

There are methods that allow a visual inspection of the power spectrum and of the fit, and those that allow a semi-automatic determination of CTF parameters using a graphical interface in case automatic procedure would fail (Zhou et al., 1996; Ludtke et al., 1999). However, there have been few attempts to sort these power spectra according to their shape in order to remove problematic micrographs, showing drift or fuzzy diffraction rings. For example, to assay local quality of cryo-EM images taken on carbon grids with thin carbon film, Gao and colleagues (Gao et al., 2002) used multivariate statistical analysis (MSA) of rotationally averaged power spectra of micrograph pieces (van Heel and Frank, 1981; Lebart et al., 1984; van Heel, 1984). They discovered significant variations in the falloff of power spectra of local areas. MSA has been also used to sort power spectra of picked particles according to similar CTF parameters (Sander et al., 2003). To suppress large signal at the center of the power spectrum and to raise signal strength in regions with fast sign changes of the CTF, images were high-pass filtered before power spectra computation, using an inverse Gaussian filter (Sander et al., 2003). Then, the average of each class of power spectra (with similar CTF parameters) was used to estimate iteratively CTF parameters. Moreover, defocus variation between neighbouring micrograph areas was investigated as a function of the area size, using test images of a specimen that was prepared employing three cryo-EM techniques (cryo-preparation in holey-carbon films, cryo-preparation on constant support carbon film, and cryo-negative staining) (Sander et al., 2003). Similarly, a global average power spectrum of masked particle images boxed from a given micrograph was used to improve the visibility of diffraction rings (Zhou et al., 1996).

A common technique for computing the global average power spectrum of a given micrograph is the technique of averaged overlapping periodograms (Welch, 1967; Fernández et al., 1997; Zhu et al., 1997). Given a finite, discrete spatial series (e.g., a digitized micrograph), one can estimate its power spectrum density (PSD) by computing the periodogram, which is the squared amplitude of the discrete Fourier transform of the series. However, the periodogram is a biased and inconsistent estimate of the power spectrum. Since, it can fluctuate a lot around the true power spectrum (the standard deviation of the estimate might have the same magnitude as the quantity being estimated), the method of averaged overlapping periodograms has been designed. This method reduces the variance of the estimate by averaging periodograms from a large number of overlapping image pieces. However, to improve the resolution of the estimate, one has to increase the size of the pieces. Thus, to approach both goals, one has to make a trade-off between the number of pieces and their size. In the area of one-dimensional signal processing, Welch showed that the variance is reduced by almost a factor of two if the overlap between the pieces is one-half of their length (Welch, 1967). In electron microscopy image processing, Zhu and colleagues proposed to reduce the variance further by computing a one-dimensional rotational average of the two-dimensional power spectrum estimate (Zhu et al., 1997). However, this radial averaging cannot be used when aiming at detecting radial asymmetry such as astigmatism or drift.

In this paper, we describe a novel method for improvement of the visibility of diffraction rings, even on images of vitreous ice without underlying carbon support film. This method relies mainly on a band-pass filtering of the two-dimensional PSD estimate obtained by averaging overlapping periodograms. We demonstrate the efficiency of this method using simulated micrographs, experimental cryo-electron micrographs of a macromolecular complex, and even using micrographs of pure (Micropore®) water on classical holey-carbon grids without additional carbon film. The main goal of this work was not to use these enhanced power spectra for accurate estimation of CTF parameters. Our goal was simply to identify drifted entire micrographs and/or defective (charged) local areas from which picked particles would introduce errors into 3D reconstruction. After having tested several approaches, we developed a very simple but efficient semi-automatic method for sorting of enhanced PSDs computed from entire micrographs and/or their local areas. This method is based on the normalized cross-correlation (NCC) between enhanced PSDs and their copies rotated by 90°. Although this criterion is meant to primarily reject drifted areas/micrographs, we use it also to remove non-diffracting (without diffraction rings) areas/micrographs that do not contain information susceptible to improve signal-to-noise ratio (SNR) of the final 3D map. If the available data set is small, we can accept non-drifted areas/micrographs diffracting poorly (with a small number of rings, sometimes, only one) because they can still increase a poor SNR. However, when a large amount of data is available, we can afford to reject images coming from such areas/micrographs. This rejection could be done visually, which is facilitated by our enhancement algorithm. Moreover, the NCC criterion for automatic rejection can be used to reject strongly astigmatic areas/micrographs when correcting the CTF with strategies that do not take into account the astigmatism.

2. Methods

2.1. Enhancement of diffraction rings

To estimate the PSD of a micrograph (or of a local area), we first divide it in a set of pieces that overlap by 50% and compute the squared amplitude of the discrete Fourier transform of each piece (i.e., periodograms). We estimate the PSD by averaging periodograms of all pieces (Fig. 1A). To improve the visibility of diffraction rings in the PSD estimate, we first apply a logarithm function (Fig. 1B), which facilitates the visualization of small amplitudes in the spectrum.

Due to a low SNR in cryo-electron micrographs, and consequently in their periodograms, it is quite common to find extremely large or small values that appear in complete discrepancy with other values in the PSD estimate. These values are outliers that prevent a correct visualization of the PSD estimate and that might bias posterior sorting. To avoid these two inconveniences, we apply an outlier rejection step comprising two standard algorithms: median filtering followed by histogram clipping (Fig. 1C).

Median filtering consists in replacing the value of each pixel by the median value of the pixels covered by a square window centered on the same pixel. For the experiment described here, the square window for median filtering was of size 3×3 pixels.

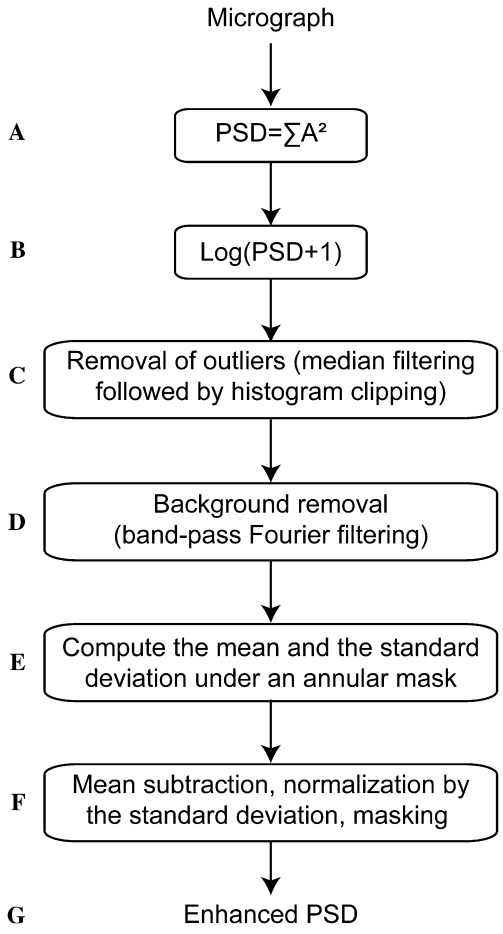

Fig. 1. Consecutive steps for computation of enhanced PSDs containing diffraction rings with significantly improved visibility.

Histogram clipping is another common outlier rejection algorithm. Given the histogram of the median-filtered image, one can compute its Lth percentile (the minimum pixel intensity giving L percent of pixels with intensities below this minimum value). We use this statistics to perform clipping of the smallest and of the highest pixel intensities. We therefore set 1% of pixels with the smallest intensities to the value determined by the 1st percentile. Similarly, we set 1% of pixels with the highest values to the value determined by the 99th percentile.

To remove the background, we then filter the image using a band-pass Fourier filter with the band [0.05, 0.2] and with a cosine edge of width 0.02 (Fig. 1D) (remark: we used here normalized frequency units where Nyquist frequency corresponds to 0.5). Note that this band-pass filter must be designed taking into account the distance between two neighbouring CTF zeros (in this paper, this distance is called "ring width" and measured in Fourier pixels), which depends on the sampling rate and on the expected defocus. For instance, if the ring width is N Fourier pixels, then the associated frequency for the band-pass filtration is $1/N$. Thus, our filtration in the frequency range between 0.05 and 0.2 is adapted to the ring widths in the range between 5 and 20 Fourier pixels. We will show further in this section an illustration of the influence of the sampling rate and of the defocus value on the ring width and on the CTF extent. In this paper, we use the term "CTF extent" to refer to the area in the power spectrum over which CTF can be detected. The size of this area depends on how far out the image diffracts.

In the next step, we compute the mean value and the standard deviation on the region defined by an annular mask with the inner radius 0.025 and with the outer radius 0.2 (both radii in normalized frequency units) (Fig. 1E). Again, this mask was defined considering the actual CTF extent. Namely, occurrence of the first diffraction ring must be taken into account by the inner radius (here 0.025) while outer diffraction rings must be included below the outer radius (here 0.2).

Finally, we use the statistics computed in Fig. 1E to normalize the processed PSD images (Fig. 1F). The normalization is done by an arithmetic modification of the intensity of each pixel, which consists in a subtraction of the mean intensity value under the mask and a subsequent division by the standard deviation value under the same mask. The resulting image (called "enhanced PSDs" throughout this paper) is finally masked using an annular mask with the same inner radius as the mask described above (0.025) but with a 10% smaller outer radius (0.18) (Fig. 1G).

To illustrate the influence of the sampling rate and of the defocus value on the width of the diffraction rings and on the CTF extent, we show in Fig. 2 the PSDs of a synthesized micrograph influenced by three different CTFs.

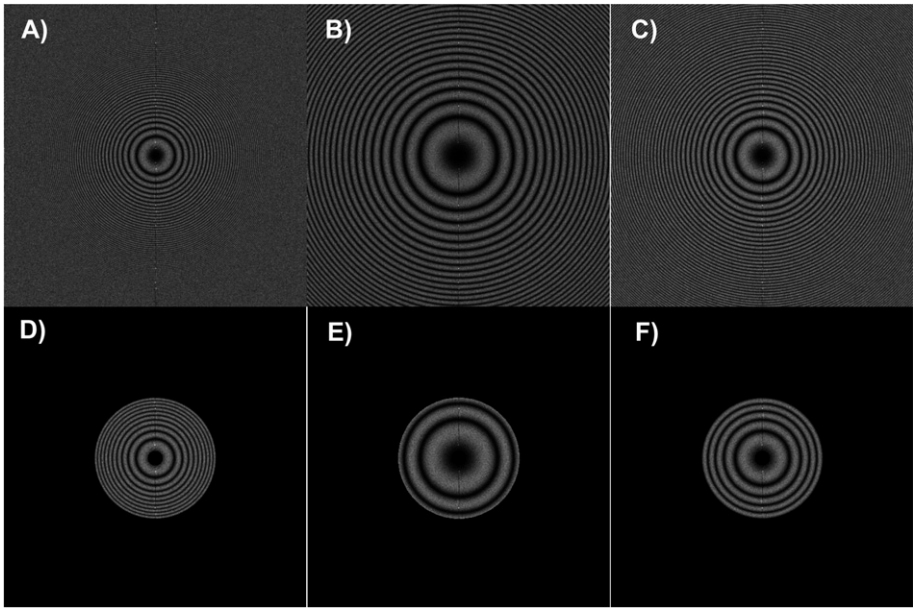

Fig. 2. Influence of pixel size and of defocus values on the width of diffraction rings and on the PSD extent. log(PSD + 1) of a synthesized, CTF-influenced micrograph for the following three combinations of pixel size and defocus: (A and D) pixel size = 1.6 Å × 1.6 Å, defocus = −2.5 μm, (B and E) pixel size = 3.2 Å × 3.2 Å, defocus = −2.5 μm, and (C and F) pixel size = 1.6 Å × 1.6 Å, defocus = −1.25 μm. A circular mask with the radius 0.025 (in normalized frequency units) was applied in (A–C). An annular mask with the inner radius of 0.025 and the outer radius of 0.2 (in normalized frequency units) was applied in (D–F). Note that these images are shown on the entire normalized frequency range (from −0.5 to 0.5).

The simulated micrograph had a size 2048 × 2048 pixels and contained no particles but only a Gaussian white noise with a standard deviation of 1. The CTFs were simulated without astigmatism using a model proposed by Velázquez-Muriel et al. (Velázquez-Muriel et al., 2003). The first CTF was simulated for a pixel size of 1.6 Å × 1.6 Å and a defocus of −2.5 μm (Fig. 2A). The second was computed for a pixel size of 3.2 Å × 3.2 Å and a defocus of −2.5 μm (Fig. 2B) while the third was simulated for a pixel size of 1.6 Å × 1.6 Å and a defocus of −1.25 μm (Fig. 2C). The other parameters of the CTF model were identical in all three cases (the acceleration voltage of 200 kV and the spherical aberration of 0.5 mm). Note that the spherical aberration coefficient and the voltage were chosen to simulate the experimental conditions on our JEOL JEM 2100F with an ultra high-resolution pole piece. Fig. 2A–C show the estimated PSDs on the whole normalized frequency range (from −0.5 to 0.5) after applying the logarithmic operator. Note that the visibility of small values was additionally improved by masking the central parts of the PSDs using a circular mask with a radius of 0.025 in normalized frequency units. From these figures, we see how the CTF extent increases as we are approaching to the focus for the same pixel size (Fig. 2C vs. Fig. 2A). Also, we see how the width of the diffraction rings increases (consequently, the CTF extent increases too) as the pixel size is increasing for the same defocus value (Fig. 2B vs. Fig. 2A). These examples indicate how one should select the size of the annular mask in Fig. 1E. The influence of the mask size on the number of diffraction rings taken into account with the mask can be seen in Fig. 2D–F, which present the images from Fig. 2A–C masked using an annular mask with the inner radius of 0.025 and the outer radius of 0.2. For instance, we took into account almost all the rings in the case of the pixel size 1.6 Å × 1.6 Å and the defocus −2.5 μm (Fig. 2D) while, using the same mask, we took into account only the first two rings in the case of a four times larger pixel (3.2 Å × 3.2 Å) and the same defocus value (Fig. 2E).

2.2. Sorting

When considering most of the effects that can affect the quality of an electron microscope image, they almost always induce some anisotropy in the PSD image. For instance, a perfect micrograph produces a set of circular diffraction rings, while astigmatism produces ellipsoidal diffraction rings. Also, thermal drift of the cryo-holder induces a truncation of diffraction rings perpendicularly to the direction of movement, as if chopped down by two parallel blades. A micrograph showing this defect has a constant drift all over its local areas. Therefore, when looking at local power spectra of such micrographs, they all show the same behaviour. Conversely, local charging effects on a frozen-hydrated sample are most likely responsible for having both drifted and non-drifted local areas within the same micrograph. In this paper, we use the term "local drift" to specify that it occurs only on some parts of a micrograph.

To detect any of these anisotropic patterns, we compared each enhanced PSD image with its own copy rotated by 90°. To perform this pair-wise comparison, we computed the normalized cross correlation (NCC) between these two images, which is a simple and fast computation.

Furthermore, we found that this measure was sufficiently discriminative to sort different PSD patterns according to their (an)isotropy. The NCC is defined as

$$\mathrm{NCC} = \max_j \frac{\sum_{\mathbf{k}} (f_{\mathbf{k}} - \overline{f})(g_{\mathbf{k}-\mathbf{j}} - \overline{g})}{\sqrt{\sum_{\mathbf{k}} (f_{\mathbf{k}} - \overline{f})^2} \sqrt{\sum_{\mathbf{k}} (g_{\mathbf{k}} - \overline{g})^2}}, \quad (1)$$

where $f_{\mathbf{k}}$ and $g_{\mathbf{k}}$ are the samples of two images at the pixel coordinate $\mathbf{k}$, and $\overline{f}$ and $\overline{g}$ are the mean values of the corresponding images. The denominator in Eq. (2) serves to normalize correlation coefficients such that $-1 \leqslant \mathrm{NCC} \leqslant 1$, $\mathrm{NCC} = 1$ indicating maximum correlation (here, ideally circular diffraction rings), $\mathrm{NCC} = 0$ no correlation, $\mathrm{NCC} = -1$ meaning that one image is the inverse of the other, and $-1 < \mathrm{NCC} < 0$ meaning that one image has small values in the same part where the other image has large values. In the ideal case of perfectly circular rings without noise, the NCC depends neither on the number of rings nor on the contrast in the spectrum ($\mathrm{NCC} = 1$ for any number of rings and for any contrast). In reality, however, noise in the spectra and imperfect circularity of the rings lead to different NCC values below 1.

The sorting based on the NCC is a semi-automatic method since one has to draw a limit to discriminate problematic micrographs/areas from usable ones. However, fixed boundaries for NCC values simplify the selection of a threshold value by the user. Moreover, a display of enhanced PSDs after being ranked according to increasing NCC values provides really a good help for selecting the threshold NCC value.

We have tested the NCC similarity measure in a fully controlled simulation environment that allowed for an objective assessment of its utility for sorting. We evaluated its dependence on the intensity of a simulated astigmatism. For this, we used the synthesized micrograph from Section 2.1 (of size 2048×2048 pixels, and containing no particles but only a Gaussian white noise with a standard deviation of 1). We computed 20 CTF-influenced micrographs by applying 20 different CTFs on the synthesized micrograph (according to the same CTF model as the one used in Section 2.1 (Velázquez-Muriel et al., 2003)). Each CTF was corresponding to a selected defocus value along the y-axis that was in the range from -2.5 to -4.4 μm, with a step of -1.0 μm. All remaining parameters of the CTF model were kept constant (defocus value along the x-axis $= -2.5$ μm; angle of astigmatism $= 0°$, acceleration voltage $= 200$ kV, spherical aberration $= 0.5$ mm, and sampling rate $= 1.59$ Å). Each of these CTF-influenced micrographs was processed using our algorithm for computation of enhanced PSDs (Fig. 1). Four out of 20 enhanced PSD images are shown in Fig. 3A–D. The intensity of astigmatism is indicated by the absolute value of the difference between the defocus values in the x- and y-directions, and it is given in the lower right corner of the respective sub-panel (0.0 μm for no astigmatism, Fig. 3A; 1.9 μm for the maximum astigmatism, Fig. 3D).

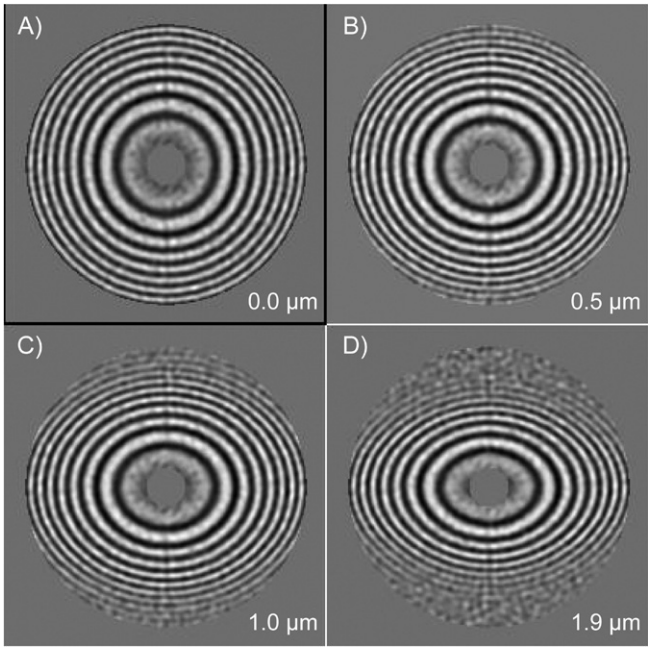

Fig. 3. Four examples of enhanced PSDs from a series computed for twenty synthesized, CTF-influenced micrographs whose defocus value along the y-axis was varying from -2.5 to -4.4 μm, with a step of -1.0 μm, while all remaining CTF parameters were constant (defocus value along the x-axis $= -2.5$ μm, angle of astigmatism $= 0°$, acceleration voltage $= 200$ kV, spherical aberration $= 0.5$ mm, and sampling rate $= 1.59$ Å). The absolute value of the difference between the defocus values in the x- and y-directions for each of four micrographs is given in the lower right corner of the corresponding sub-panel.

Then, we computed the NCC between these images and their copies rotated by 90°. For instance, the NCC for the image with no astigmatism was 0.97. We show in Fig. 4 the NCC as a function of the intensity of astigmatism. Note that the NCC falls below 0.5 as soon as the intensity of astigmatism increases above approximately 0.15 μm. The NCC for each of the tested discrete defocus differences is denoted by a cross. The numbers above the crosses indicate images (from 1 to 20, 1 stands for the image with no astigmatism, 20 stands for the image with the maximum astigmatism) that were ranked according to decreasing NCC values. We see that PSDs were perfectly sorted according to the intensity of astigmatism for the intensities below approximately 0.8 μm. For a stronger astigmatism than 0.8 μm, three images (9, 10, and 11) were wrongly ranked. In these three cases, however, the NCC had very small values (lower than 0.12). The error of 0.03 for the image with no astigmatism as well as a wrong sorting of three images with the astigmatism stronger than 0.8 μm (and with $\mathrm{NCC} < 0.12$) mainly come from the noise that is present in the spectrum. This noise is mostly visible on the first diffraction ring in the enhanced PSDs (Fig. 3A–D). We can also see that very astigmatic spectra have a much lower SNR in the domain of high frequencies than in the domain of low frequencies (Fig. 3C and D). This means that we introduce more noise into computation of the NCC in case of such spectra because we compute the NCC using the

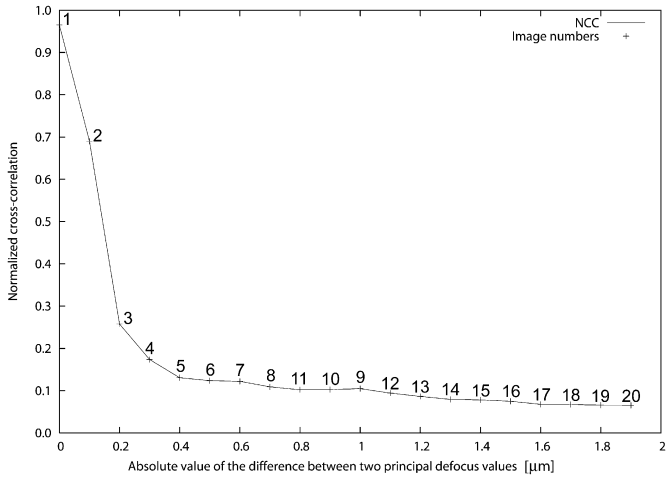

Fig. 4. Assessment of quality of the NCC similarity measure for sorting purposes, in a fully controlled simulation environment. NCC as a function of the absolute value of the difference between the defocus values in the x- and y-directions. The NCC value for any of 20 tested defocus differences (from 0 to 1.9 μm) is marked by a cross. The numbers of PSDs ranked according to decreasing NCC values are displayed above the crosses. Ideally, the image numbers should be ranked in ascending order (from 1 to 20) as the absolute value of the difference between the two principal defocus values increases from 0 to 1.9 μm.

entire enhanced PSD image covered by the annular mask. This noise may cause a wrong sorting of images with low NCC values such as our three images with NCC < 0.12. Another potential sources of errors are imperfections of the PSD estimate that can be made during periodogram averaging (quality of the estimate depends on the number of averaged periodograms and on the box size). Also, the centering of the spectra may produce artifacts (for example, a vertical central line that is visible in each sub-panel of Fig. 3). They mean that we may not be able to simulate the perfect isotropy even in the ideal case with no noise (the maximum NCC would be slightly lower than 1). This analysis suggests that we should generally reject images with the NCC below 0.12 because we cannot trust the sorting results for such low NCC values.

We have also tested a few other criterions (such as the cross-correlation index, the covariance, and the Euclidian distance) to see how they sort enhanced PSD images with simulated astigmatism. However, the ranking using these criterions was less correct than when using the NCC criterion.

3. Experiments

3.1. Glutamate synthase (GltS) data set

The specimen used in these experiments is glutamate synthase (GltS), which is a multienzymatic complex formed with glutamine synthetase, the main ammonia assimilation pathway in microorganisms and plants. The GltS sample was diluted at a concentration of 9.25 mg/ml (30 μM), in a Hepes/KOH 25 mM, pH 7.5, buffer with EDTA 1 mM, DTT 1 mM. A droplet of 5 μl of sample solution was applied on a 400-mesh copper grid, coated with a thin holey-carbon film. After blotting the excess of solution with Whatman paper, the grid was rapidly plunged into liquid ethane and transferred under liquid nitrogen into the microscope using a side entry nitrogen-cooled Gatan 626 cryoholder (Dubochet et al., 1982). Images in a defocus range from −1.7 to −3.2 μm were recorded on a JEOL JEM 2100F with an ultra high-resolution pole piece, without tilt, with an acceleration voltage of 200 kV, a spherical aberration of 0.5 mm, and a magnification of 50000×. Images were recorded under low dose conditions (10 electrons per A^2) on Kodak SO 163 films. Micrographs were digitized on a Nikon Coolscan 8000ED microdensitometer with a pixel size equivalent to a 1.59 Å × 1.59 Å square on the sample scale. The final 3D map of the GltS obtained from this data set corresponds to a global resolution of less than $FSC_{0.5} = 9.5$ Å (in preparation for publication by Cottevieille et al.).

3.2. Performances of the PSD enhancement algorithm

3.2.1. Enhanced PSDs of the GltS complex

In the experiments on entire micrographs of the GltS complex, we achieved a good trade off between the resolution of the PSD estimate and its variance reduction using a box size of 512 × 512 pixels. This box size produced about 1000 periodograms per micrograph. To visually check the effect of our PSD enhancement algorithm, we selected the averaged power spectrum of an isotropic and of an anisotropic micrograph (Fig. 5A and B, respectively). Note that the isotropic spectrum was selected arbitrarily (as we will see later, it is actually not the spectrum of the best quality computed for the available data set). To help the visualization of small amplitudes, we applied a circular mask with a radius of 0.025 (in normalized frequency units) on the central area of the raw averaged power spectra. Despite this precaution, Fig. 5A and B reveal only the first two diffraction rings, although weak. The remaining rings start faintly appearing only after applying the logarithmic operator (Fig. 5C and D). However, they become easily visible after applying the successive steps of our enhancement algorithm (Fig. 5E and F). Moreover, these enhanced PSDs facilitate the quality assessment of micrographs. In our example, to say whether the two micrographs are isotropic or anisotropic, or which kind of anisotropic features they contain (astigmatism or drift), it is easier to inspect Fig. 5E and F than A and B or C and D. Thus, by looking at the enhanced PSDs, we can easily see that the micrograph corresponding to Fig. 5E is isotropic since it displays a nice circular pattern while the micrograph corresponding to Fig. 5F is drifted as its enhanced PSD contains truncated diffraction rings. Note that, from Fig. 5 on, we show only a central part of PSD images, which is covered by the annular mask. Therefore, the size of all the remaining PSD figures in this paper is 212 × 212 pixels (remark: 212/2 = 106 pixels, which corresponds to a normalized fre-

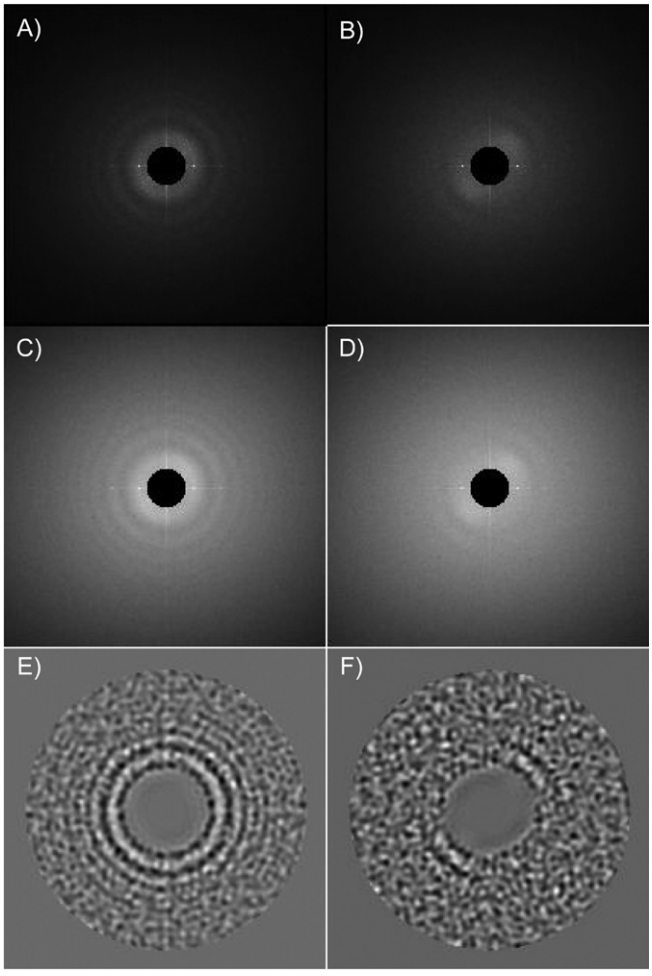

Fig. 5. PSD enhancement for two micrographs of the glutamate synthase complex on classical holey-carbon grids without additional carbon film. (A and B) Raw PSDs. (C and D) log(PSD + 1). (E and F) PSDs enhanced using the algorithm from Fig. 1. A circular mask with a radius of 0.025 (in normalized frequency units) was applied in (A–D) to mask the central area. An annular mask with the inner radius of 0.025 and the outer radius of 0.18 (in normalized frequency units) was applied in (E and F) as a part of the enhancement algorithm. Note that only a central image part is shown in (A–F), which corresponds to the normalized frequency range from −0.21 to 0.21.

quency of 0.21 and, for the data set used here, to a spatial frequency of 1/7.6 $Å^{-1}$).

3.2.2. Enhanced PSDs of buffer or water alone

Since the visibility of diffraction rings seemed to be greatly improved by our enhancement algorithm, we decided to test it in two extreme conditions. First, we computed enhanced PSDs for a defocus series of six cryo-electron micrographs recorded in similar cryo-EM conditions as with the GltS complex, but only with the buffer solution used for recording the GltS images (enhanced PSDs of four out of six micrographs of the buffer are shown in Fig. 6). These images were collected in strongly controlled imaging conditions. One of our goals was also to simulate imperfect conditions in one of the shots. Thus, we simulated a weak drift in one of the images by touching the column of the

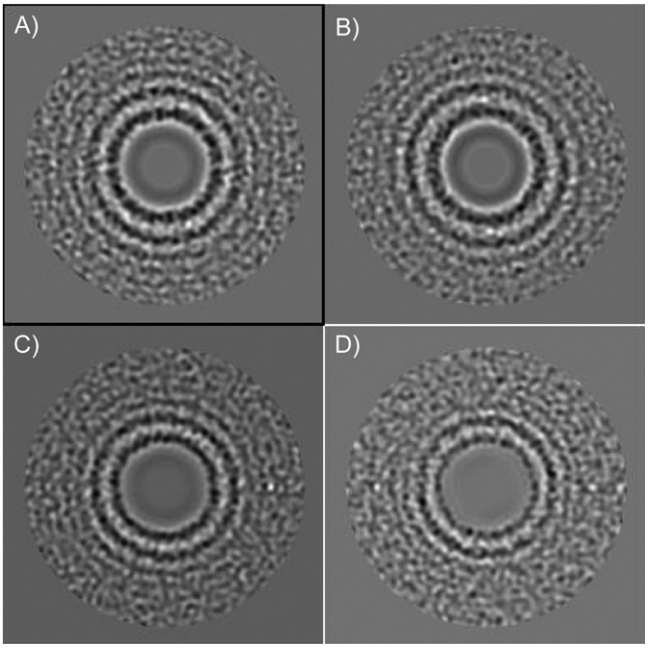

Fig. 6. Enhancement of PSDs in case of a low concentration of diffracting material. Four out of six enhanced PSDs computed for a defocus series of cryo-electron micrographs recorded in similar cryo-EM conditions as with the glutamate synthase complex, but using its buffer alone.

microscope (Fig. 6D). As the reader can see, the visibility of diffraction rings is very strong in Fig. 6A–C and it is slightly weaker in case of Fig. 6D. The composition of the buffer solution was quite common and its ionic strength was small (25 mM KOH).

Encouraged by this first result, we made a second test using a defocus series of six cryo-electron micrographs of Micropore® water alone on the cryo-EM grid. This time the success rate was lower as only three enhanced PSDs out of six showed distinct diffraction rings. Two out of three enhanced PSDs showing no visible rings are presented in Fig. 7A and B while two out of three enhanced PSDs showing visible rings are given in Fig. 7C and D. At first sight, we could not explain why certain areas of pure vitreous ice were producing diffraction patterns while, on the same grid and in similar experimental conditions, other areas could not. However, after checking micrographs and the experimental conditions at the electron microscope, we concluded that ice thickness was responsible for producing visible diffraction rings. Indeed, the JEOL 2100F electron microscope is equipped with fluorescent screens that can detect and measure the intensity of the electron beam in the projection chamber. After recording an image, we expose usually the same sample area again to measure the intensity of the electron beam transmitted through the sample. This time, it turned out that the vitreous ice which did not produce diffraction rings corresponded to a transmitted current density of 7.9 pA/cm^2 (Fig. 7A), 8.5 pA/cm^2, and 9.1 pA/cm^2 (Fig. 7B). Conversely, the holes with vitreous ice producing diffraction rings corresponded to a transmitted current density of 10.5 pA/cm^2

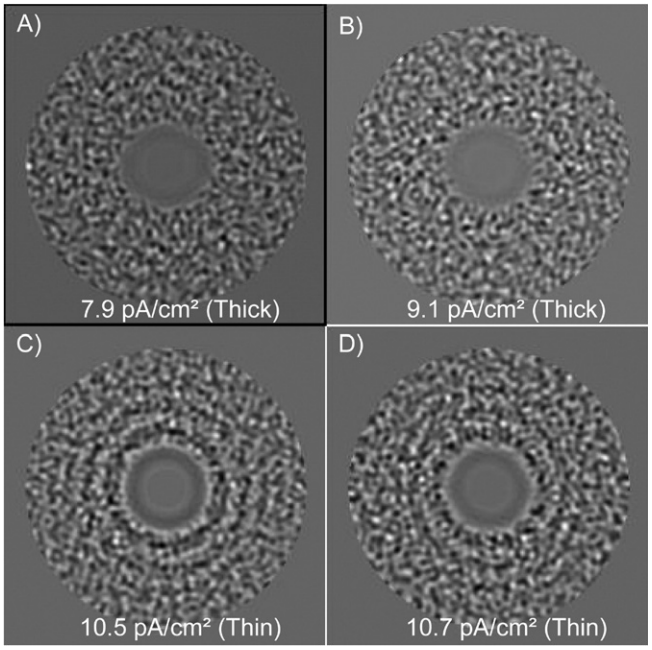

Fig. 7. Enhancement of PSDs of six cryo-electron micrographs recorded in similar cryo-EM conditions as with the glutamate synthase complex, but using pure water. Influence of ice thickness (the respective current densities transmitted through ice are indicated in each sub-panel). (A and B) Two out of three enhanced PSDs coming from thick ice. (C and D) Two out of three enhanced PSDs coming from thin ice.

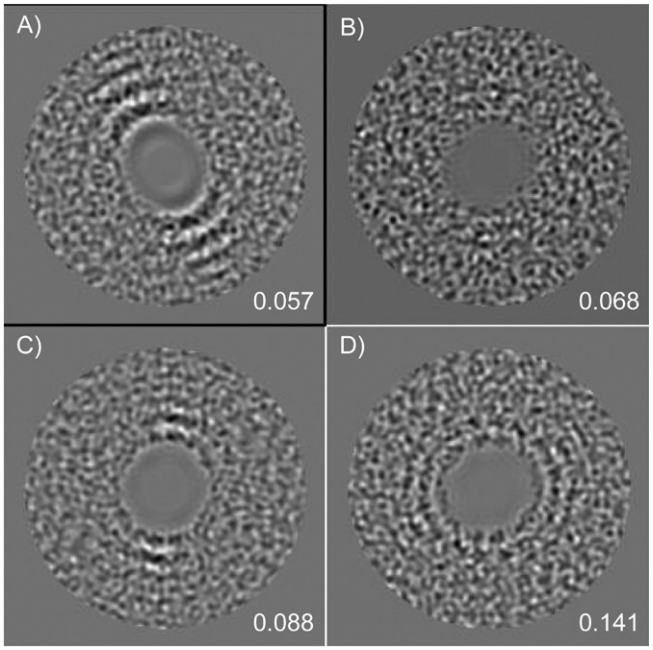

Fig. 8. Four out of 16 global enhanced PSDs of the glutamate synthase complex that were sorted as having the lowest NCC values (from 0.057 to 0.141), presenting drift (A and C), invisible diffraction rings (B), or a strong astigmatism (D).

(Fig. 7C), 10.6 pA/cm^2, and 10.7 pA/cm^2 (Fig. 7D), and holes without vitreous ice corresponded to approximately 13.5 pA/cm^2. Knowing that a bigger amount of transmitted current indicates a thinner ice, we concluded that the enhanced PSDs in Fig. 7A and B originated from thick ice while those in Fig. 7C and D were produced by thin ice. Although these values do not provide an accurate measurement of ice thickness, they strongly suggest that vitreous ice of pure water must be sufficiently thin to be able to produce visible diffraction rings.

We can notice a difference between Figs. 6 and 7 leading to the question of why a buffer solution produces diffraction rings of a better quality than pure water. A buffer solution contains diffracting materials that pure water does not. Thanks to their diffraction, quality of the spectra is better than in case of pure water. Also, a different SNR in two figures (the SNR is much lower in Fig. 7 than in Fig. 6) makes visualization different in the two cases.

3.3. Sorting using 90° rotated PSDs

3.3.1. Sorting of entire micrographs

We first computed the enhanced PSDs of 151 whole micrographs of the GltS complex (Section 3.1). Then, we cross-correlated each enhanced PSD with its 90° rotated copy, and ranked them according to their increasing NCC values. We shown in Fig. 8A–D four out of 16 PSDs associated with the lowest NCC values (from 0.057 to 0.141). They apparently correspond to drifted micrographs (Fig. 8A and C), micrographs devoid of visible diffraction rings (Fig. 8B), and micrographs with a strong astigmatism (Fig. 8D). According to our selection criterion, micrographs with invisible or drifted rings should not be used for 3D reconstruction while astigmatic micrographs may be used when applying strategies that can correct the astigmatism.

Conversely, 16 PSDs with the highest NCC values (from 0.580 to 0.726) have clearly visible circular diffraction rings and show no visible signs of anisotropy. Four of them are shown in Fig. 9A–D. Except for one image (Fig. 9B), where only one ring is visible, all the other micrographs show some signal up to the high spatial frequencies delineated by the annular mask (outer radius of 0.18 in normalized frequency units, which corresponds to a spatial frequency of 1/8.83 Å^{-1} for the data set used in this paper). Note that the maximum NCC value is only 0.726 (Fig. 9D) while it was 0.97 in case of simulated isotropic images. The main reason for this difference is a much lower real SNR, which makes imperfections of the PSD estimate stronger than those in the simulated case. These imperfections seem also to be enhanced after processing of the PSDs using our enhancement algorithm (Fig. 5C and D vs. Fig. 5E and F).

After ranking enhanced PSDs according to increasing NCC values, it becomes easy to draw a discriminating line between isotropic and anisotropic images. Moreover, if a sufficient amount of data is present, one can also raise his/her standard of quality accordingly by selecting a higher discriminating threshold NCC value. By visual inspection, we selected a NCC value of 0.275 as the threshold below which 35 GltS micrographs were sorted

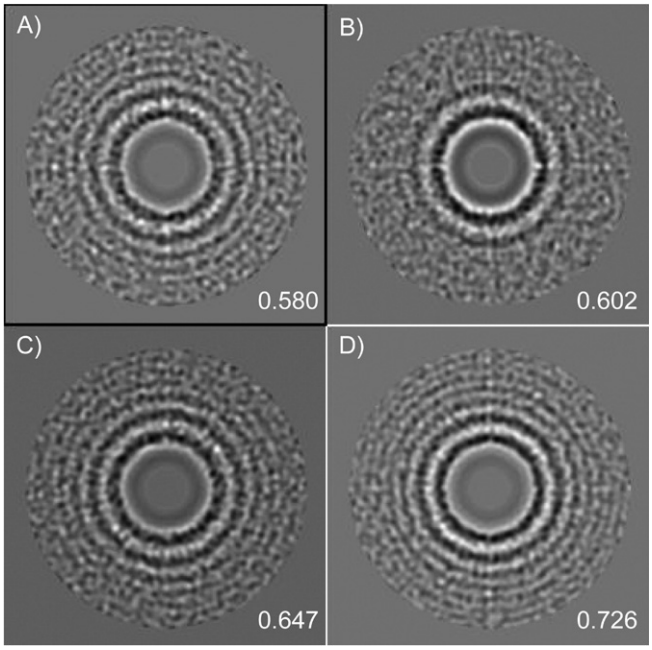

Fig. 9. Four out of 16 global enhanced PSDs of the glutamate synthase complex that were sorted as having the highest NCC values (from 0.580 to 0.726), presenting no visible sign of anisotropy.

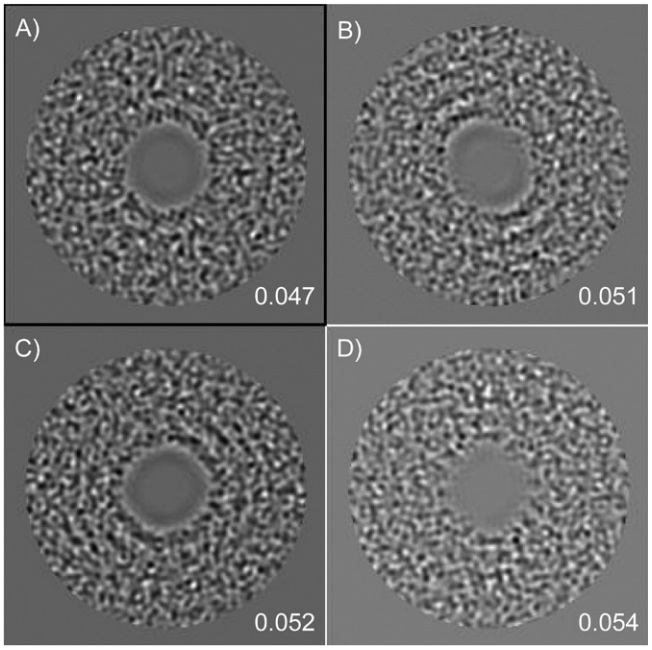

Fig. 10. Four out of 16 local enhanced PSDs of the glutamate synthase complex that were sorted as having the lowest NCC values (from 0.047 to 0.054), presenting drift (A–C) or no visible diffraction rings (D).

as anisotropic. Using this fast and simple tool, we successfully sorted 142 out of 151 entire GltS micrographs (the accuracy of sorting was assessed by visual inspection). This experiment showed therefore that the NCC could be used as an efficient tool in sorting PSDs with a low SNR.

As expected, a few micrographs were uneasy to sort as isotropic or anisotropic as a whole. We supposed that some micrographs were heterogeneous and could simultaneously have some isotropic and some anisotropic local areas. Also, averaging of local spectra with different defocus values may lead to an anisotropic spectrum and, consequently, to a low NCC value. To detect main defocus variations within micrographs as well as local drift, we propose inspection of local areas beside inspection of entire micrographs.

3.3.2. Sorting of local areas

We started this study by determining the minimum size of local areas producing the spectra of size 512×512 pixels of a quality that was acceptable for sorting purposes. It turned out that this size was 3840×3840 pixels, which corresponded to 15×15 overlapping sub-areas of size 512×512 pixels for periodogram averaging. We then divided each GltS micrograph into four, five, or six local areas, depending on the size of the micrograph. This made a total of 866 local areas or 866 corresponding enhanced PSDs to be sorted. The NCC between each local enhanced PSD and its 90° rotated copy was again used to rank the images. One-half of the 16 PSDs associated with the lowest NCC values now corresponds to strongly drifted images (three different directions of drift are presented in Fig. 10A–C) while the other half shows hardly visible diffraction rings (an example is shown in Fig. 10D). When comparing these images with the enhanced PSDs computed on whole micrographs (Fig. 8), we see that they clearly have a lower SNR, but the signal is still strong enough for checking anisotropic features.

Similarly, 16 enhanced PSDs with the highest NCC values (four of them are shown in Fig. 11A–D) seem noisier than the ones computed from whole micrographs (Fig. 9). Hence, the highest NCC value is now only 0.525 while it was 0.726 previously. Nevertheless, the isotropy of the enhanced PSDs is still very good, though diffraction rings are less easy to spot. We selected a NCC value of 0.12 (minimum acceptable value of the threshold according to Section 2.2) as the threshold value separating 547 isotropic from 319 anisotropic areas. A visual inspection revealed 38 ambiguously sorted areas out of 866 with this single threshold approach, which is still a success rate of 95.6%.

To better understand how local and global PSDs could produce contradictory results, we checked the PSDs of local areas originating from the same micrographs. In most cases, the areas were uniformly isotropic or uniformly anisotropic. However, in almost 30% of the micrographs, both behaviours were simultaneously visible. Indeed, when considering the origins of the anisotropic local areas, it turned out that 155 out of 319 anisotropic areas came from 33 micrographs sorted as anisotropic while the remaining 164 anisotropic local areas came from 49 micrographs sorted as isotropic in Section 3.3.1.

For instance, we shown in Fig. 12 local enhanced PSDs of a micrograph, of which the global enhanced PSD is shown in Fig. 5E. Two areas located at the right-hand side

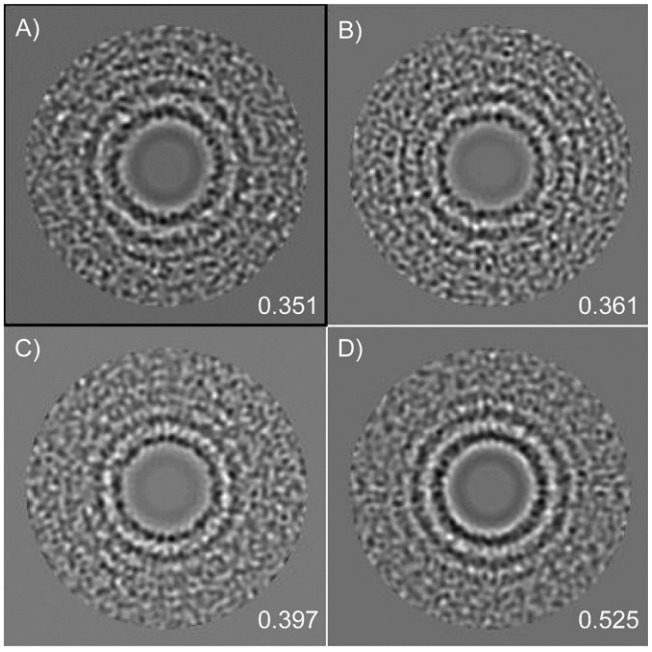

Fig. 11. Four out of 16 local enhanced PSDs of the glutamate synthase complex that were sorted as having the highest NCC values (from 0.351 to 0.525), presenting no visible sign of anisotropy.

of this micrograph seem to have a good degree of isotropy (Fig. 12C and F) but there seems to be also a gradient of anisotropy towards the left-hand side of the micrograph producing the areas from slightly drifted (Fig. 12A, B, and E) to strongly drifted (Fig. 12D). We could therefore say that the right-hand side of this micrograph is good but that there is also some charging effect inducing a strong drift near the lower-left corner of the micrograph. This local drift is however not visible in the global enhanced PSD (Fig. 5E). Thus, it is only when using local PSD assessment that one can detect such anisotropic features. However, since both local and global PSDs convey important information, we recommend examination of both.

4. Conclusions

We presented a novel strategy for improvement of the visibility of diffraction rings in the power spectrum density (PSD) image for sorting cryo-electron micrographs and their local areas. The purpose of this sorting is to identify diffracting areas containing information that will not introduce errors in 3D reconstruction. Although relatively simple, the normalized cross-correlation (NCC) between the enhanced PSDs and their copies rotated by 90° proved to be a fast and reliable way to distinguish anisotropic PSDs from isotropic ones. The NCC-based sorting is a semi-automatic method since it requires the user to set a threshold below which micrographs or their areas will be rejected. However, it is fast and easy to deal with since it is not parametric. Moreover, a display of enhanced PSDs ranked according to increasing NCC values facilitates interpretation of sorting results by the experimenter. We tested the method using synthetic images as well as using cryo-electron micrographs of glutamate synthase complex on conventional holey-carbon grids without additional carbon film. We successfully sorted 142 out of 151 micrographs and 828 out of 866 local areas, and demonstrated the coexistence of isotropic and anisotropic local areas on around 30% of micrographs.

Also, we showed the performances of our method for enhancement of diffraction rings on cryo-electron

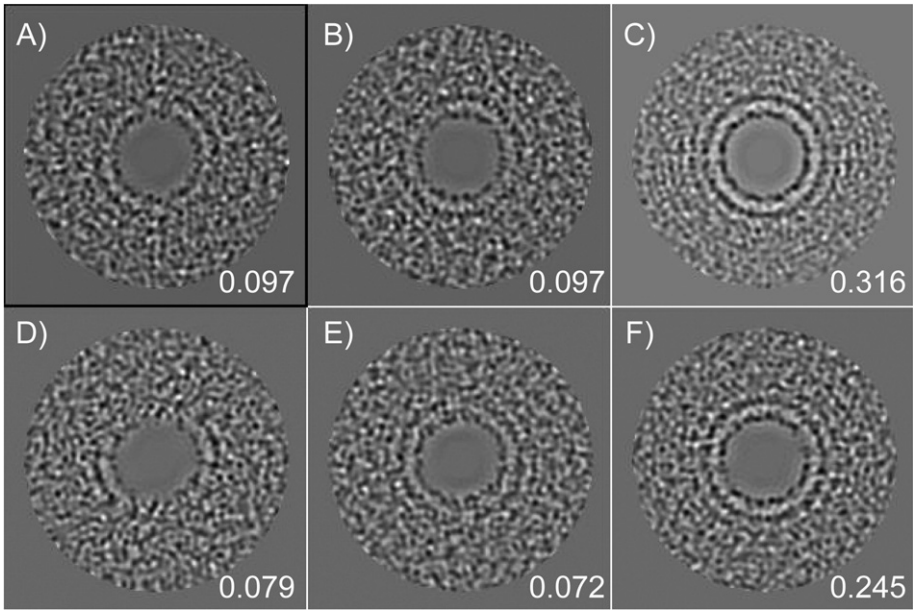

Fig. 12. Local enhanced PSDs of a micrograph whose global enhanced PSD is shown in Fig. 5E. Six enhanced PSDs corresponding to six local areas of the micrograph, with associated NCC values (from 0.072 to 0.316). Note that the drift present in local enhanced PSDs is not visible in the global enhanced PSD.

micrographs of a buffer solution as well as on those of pure water. These tests show that a buffer solution still produces clearly visible diffraction rings in absence of protein. Conversely, the experiments with pure water show that ice thickness has the greatest influence on the visibility of diffraction rings. These results recommend the use of thin ice for 3D reconstruction since it produces visible rings while thick ice does not. At first sight, it seems counterintuitive that thin ice provides better diffraction patterns than thick ice. However, we may perhaps explain it by "defocus spread effect", which could cause the resulting power spectrum to be an average of power spectra with different defocuses corresponding to different layers of vitreous ice. Shifted oscillations of the corresponding CTF curves would thus cancel each other at high spatial frequencies. They would also attenuate the resulting CTF envelope at low spatial frequencies and, consequently, reduce the signal-to-noise ratio at these frequencies. We are going to explore this possibility in the future work.

Our algorithm for diffraction rings enhancement is freely available as a part of the Xmipp image processing package (Sorzano et al., 2004) and is also freely available for implementing in other image processing packages.

Acknowledgments

We are grateful to European Commission for NoE "3D-EM" contract No. LSHG-CT-2004-502828, and to Region Ile-de-France for convention SESAME 2000 E 1435 supporting cryo-electron microscopy and JEOL 2100F installed at IMPMC. This work has been partially supported by the "Comunidad de Madrid" Grant CAM/GR/SAL/0234.

References

Carragher, B., Kisseberth, N., Kriegman, D., Milligan, R.A., Potter, C.S., Pulokas, J., Reilein, A., 2000. Leginon: an automated system for acquisition of images from vitreous ice specimens. J. Struct. Biol. 132, 33–45.

Conway, J.F., Steven, A.C., 1999. Methods for reconstructing density maps of "single" particles from cryoelectron micrographs to subnanometer resolution. J. Struct. Biol. 128, 106–118.

Cottevieille, M., Larquet, E., Jonic, S., Petoukhov, M.V., Dossena, L., Svergun, D.I., Vanoni, M.A., Boisset, N. Structural study of bacterial glutamate synthase complex by 3D cryo-electron microscopy, homology modelling, and small-angle X-ray scattering. (in preparation).

Dubochet, J., Lepault, J., Freeman, R., Berriman, J.A., Homo, J.-C., 1982. Electron microscopy of frozen water and aqueous solutions. J. Microsc. 128, 219–237.

Fernández, J.-J., Sanjurjo, J.R., Carazo, J.-M., 1997. A spectral estimation approach to contrast transfer function detection in electron microscopy. Ultramicroscopy 68, 267–295.

Frank, J., 1996. Three-Dimensional Electron Microscopy of Macromolecular Assemblies. Academic Press, San Diego.

Gao, H., Spahn, C.M., Grassucci, R.A., Frank, J., 2002. An assay for local quality in cryo-electron micrographs of single particles. Ultramicroscopy 93, 169–178.

Grob, P., Cruse, M.J., Inouye, C., Peris, M., Penczek, P.A., Tjian, R., Nogales, E., 2006. Cryo-electron microscopy studies of human TFIID: conformational breathing in the integration of gene regulatory cues. Structure 14, 511–520.

Hanszen, K.-J., 1971. The optical transfer theory of the electron microscope: fundamental principles and applications. Adv. Opt. Microsc. 4, 1–84.

Hawkes, P.W., 1992. The electron microscope as a structure projector. In: Frank, J. (Ed.), Electron Tomography. Plenum, New York, pp. 17–38.

Huang, Z., Baldwin, P.R., Mullapudi, S., Penczek, P.A., 2003. Automated determination of parameters describing power spectra of micrograph images in electron microscopy. J. Struct. Biol. 144, 79–94.

Lebart, L., Morineau, A., Warwick, K.M., 1984. Multivariate Descriptive Statistical Analysis. Wiley, New York.

Lenz, F., 1971. Transfer of image formation in the electron microscope. In: Valdre, U. (Ed.), Electron Microscopy in Material Science. Academic Press, New York, pp. 540–568.

Lepault, J., Booy, F.P., Dubochet, J., 1983. Electron microscopy of frozen biological suspensions. J. Microsc. 129 (Pt. 1), 89–102.

Ludtke, S.J., Baldwin, P.R., Chiu, W., 1999. EMAN: semiautomated software for high-resolution single-particle reconstructions. J. Struct. Biol. 128, 82–97.

Mallick, S.P., Carragher, B., Potter, C.S., Kriegman, D.J., 2005. ACE: automated CTF estimation. Ultramicroscopy 104, 8–29.

Mindell, J.A., Grigorieff, N., 2003. Accurate determination of local defocus and specimen tilt in electron microscopy. J. Struct. Biol. 142, 334–347.

Nicholson, W.V., Glaeser, R.M., 2001. Review: automatic particle detection in electron microscopy. J. Struct. Biol. 133, 90–101.

Penczek, P.A., Frank, J., Spahn, C.M., 2006a. A method of focused classification, based on the bootstrap 3D variance analysis, and its application to EF-G-dependent translocation. J. Struct. Biol. 154, 184–194.

Penczek, P.A., Yang, C., Frank, J., Spahn, C.M., 2006b. Estimation of variance in single-particle reconstruction using the bootstrap technique. J. Struct. Biol. 154, 168–183.

Potter, C.S., Chu, H., Frey, B., Green, C., Kisseberth, N., Madden, T.J., Miller, K.L., Nahrstedt, K., Pulokas, J., Reilein, A., Tcheng, D., Weber, D., Carragher, B., 1999. Leginon: a system for fully automated acquisition of 1000 electron micrographs a day. Ultramicroscopy 77, 153–161.

Radermacher, M., Ruiz, T., Wieczorek, H., Gruber, G., 2001. The structure of the V(1)-ATPase determined by three-dimensional electron microscopy of single particles. J. Struct. Biol. 135, 26–37.

Sander, B., Golas, M.M., Stark, H., 2003. Automatic CTF correction for single particles based upon multivariate statistical analysis of individual power spectra. J. Struct. Biol. 142, 392–401.

Sorzano, C.O., Marabini, R., Velazquez-Muriel, J., Bilbao-Castro, J.R., Scheres, S.H., Carazo, J.M., Pascual-Montano, A., 2004. XMIPP: a new generation of an open-source image processing package for electron microscopy. J. Struct. Biol. 148, 194–204.

Spence, J., 1988. Experimental High-Resolution Electron Microscopy. Oxford Univ. Press, New York.

Tani, K., Sasabe, H., Toyoshima, C., 1996. A set of computer programs for determining defocus and astigmatism in electron images. Ultramicroscopy 65, 31–44.

vanHeel, M., 1984. Multivariate statistical classification of noisy images (randomly oriented biological macromolecules). Ultramicroscopy 13, 165–183.

van Heel, M., Frank, J., 1981. Use of multivariate statistics in analysing the images of biological macromolecules. Ultramicroscopy 6, 187–194.

Velázquez-Muriel, J.A., Sorzano, C.O., Fernandez, J.J., Carazo, J.M., 2003. A method for estimating the CTF in electron microscopy based on ARMA models and parameter adjustment. Ultramicroscopy 96, 17–35.

Wade, R.H., 1992. A brief look at imaging and contrast transfer. Ultramicroscopy 46, 145–156.

Welch, P.D., 1967. The use of fast Fourier transform for the estimation of power spectra: a method based on time averaging over short, modified periodograms. IEEE Trans. Audio Electroacoust. AU-15, 70–73.

Zhang, P., Beatty, A., Milne, J.L., Subramaniam, S., 2001. Automated data collection with a Tecnai 12 electron microscope: applications for molecular imaging by cryomicroscopy. J. Struct. Biol. 135, 251–261.

Zhou, Z.H., Hardt, S., Wang, B., Sherman, M.B., Jakana, J., Chiu, W., 1996. CTF determination of images of ice-embedded single particles using a graphics interface. J. Struct. Biol. 116, 216–222.

Zhu, J., Penczek, P.A., Schroder, R., Frank, J., 1997. Three-dimensional reconstruction with contrast transfer function correction from energy-filtered cryoelectron micrographs: procedure and application to the 70S *Escherichia coli* ribosome. J. Struct. Biol. 118, 197–219.

Zhu, Y., Carragher, B., Glaeser, R.M., Fellmann, D., Bajaj, C., Bern, M., Mouche, F., de Haas, F., Hall, R.J., Kriegman, D.J., Ludtke, S.J., Mallick, S.P., Penczek, P.A., Roseman, A.M., Sigworth, F.J., Volkmann, N., Potter, C.S., 2004. Automatic particle selection: results of a comparative study. J. Struct. Biol. 145, 3–14.

Zhu, Y., Carragher, B., Kriegman, D.J., Milligan, R.A., Potter, C.S., 2001. Automated identification of filaments in cryoelectron microscopy images. J. Struct. Biol. 135, 302–312.